Influence of Surrounding Powder Bed and Build Platform on Thermal Cooling Characteristics in 3D Printed Parts via Selective Laser Melting

S. Feih[1], C.N. Sun[1], B. Zhang[1], Q.L. Lo[2], C. Chin[3] and J. Wei[1]

[1]Singapore Institute of Manufacturing Technology (SIMTech), 73 Nanyang Drive, 637662, Singapore
[2]Nanyang Technological University, School of Mechanical and Aerospace Engineering, 50 Nanyang Avenue, 639798, Singapore
[3]Dassault Systèmes Simulia Corp, 1301 Atwood Avenue, Johnston, RI 02919, USA

***Abstract**: Selective laser melting (SLM) leads to high cooling rates and correspondingly high residual stresses, which can distort the printed part on the printing platform and even lead to part cracking and consequent print failure. The temperature profile and cooling rates during the SLM process are influenced by the surrounding powder bed and building platform, which can act as a significant heat sink depending on part design and platform arrangement. The new functionality of the Abaqus additive manufacturing simulation framework allows for separate modelling of solid (laser exposed) material, powder bed (not exposed) and platform (not exposed), as well as evolving heat transfer surfaces for the AM part. In this paper we highlight the influence of the surrounding powder bed and platform on the thermal characteristics of the printed part. We undertake detailed investigations regarding the temperature characteristics with separate meltpool and nodal flux process simulation with regard to mesh size and increment size. We additionally investigate the potential of simplified modelling approaches to reduce the additional computational time by including the surrounding powder bed using equivalent thermal boundary conditions on the printed part. The presented simulation outcomes increase our understanding of the fundamental heat transfer processes during additive manufacturing, and the findings are also considered transferrable to other powder bed printing processes. The temperature predictions are also able to further explain microstructural and material property changes in printed Inconel 718 cylinders at varying build height and with increasing part build diameter.*

***Keywords**: Selective laser melting, powder bed processes, temperature gradients*

1. Introduction

Additive manufacture (AM) revolutionises the way components can be designed. Advanced design freedom results in a requirement for more advanced virtual design to avoid premature failure of components and to achieve maximum weight savings. Additive manufacture is a still evolving manufacturing process as improved manufacture is achieved through continuous increases in power input and scanning speed as well as increases in build chamber size and hence allowable component size. The application of metal AM is also expanding continuously to a wider range of alloys being selected for the process.

As part of SIMTech's on-going efforts in additive manufacturing research, we utilize selective laser melting (SLM) for printing of Inconel 718 metal parts. The SLM build process is characterized by rapid cooling rates due to inherently large temperature differences between the build platform and the powder particles which are melted into a solid material layer-by-layer via laser exposure during the manufacturing process. It has been experimentally established that the resulting microstructure (and hence cooling rates) depend on the build thickness and build height. Questions remain regarding the underlying mechanisms of heat transfer, resulting material properties and hence optimum process parameters.

A schematic of the heat transfer processes present during the SLM process is shown in Figure 1. The laser heats the top surface of the powder. Heat is conducted from the top layer into the base plate, which is serving as a heat sink. The base plate may be preheated to temperatures up to 200°C to control the resulting cooling rates. Heat is also conducted into the surrounding unmelted powder particles, but at a much slower rate due to the low thermal conductivity of the metallic powder. Lastly, argon gas is pumped to flow over the top surface at room temperature, which enables additional heat to be carried away via convection and radiation to the cooler surrounding.

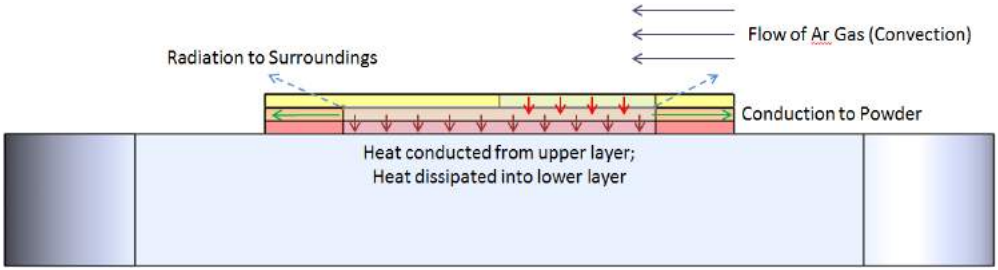

Figure 1. Heat transfer details during SLM build process

The SLM processing time increases with build height due to the layer-by-layer approach. In order to avoid costly trial-and-error print jobs for every new part, simulation tools with reasonable computational speed need to be validated against existing experimental data. In this paper we focus on the fundamental understanding of the influence of numerical parameters such as mesh

size, increment size and heat source modelling approach on the heat transfer analysis and resulting temperature gradients. Two heat source modelling approaches are compared in this paper: (1) the computationally efficient equivalent nodal flux approach working with a relatively coarse mesh with distribution of the laser heat flux to the respective top surface nodes and (2) the more detailed Goldak model (and therefore computationally slower) requiring a very fine mesh in the order of each deposited layer thickness to discretize the volume affected by the through-thickness and in-plane heat distribution. With this understanding, we investigate the effects of surrounding powder material and build platform on the established temperature profiles to recommend guidelines for best modelling practice. As temperature predictions are the main input for the stress analysis, it is crucial to understand any potential inaccuracies introduced by the necessary simplifications in order to advance the computational speed. Lastly, we utilize the numerical results to establish the differences in cooling rates for build height and build dimensions and compare these findings to experimental data.

2. Experimental Details

2.1 Cylinder Geometries

For this work, the microstructure of three cylindrical geometries (namely, D=5mm, D=10mm and D=15mm) with a build height of 320mm is experimentally investigated as a function of height and build volume. The specimen dimensions are given in Table 1. Microstructure evaluation was undertaken through polishing, etching and microscopic image analysis at selected build heights for all three cylinders. Changing the diameter for cylindrical specimens results in a lower surface-to-volume ratio, and will therefore change the heat transfer characteristics as heat input scales with the volume of the structure, but heat loss is surface controlled.

Table 1. Specimen dimensions

Diameter (mm)	Build Height (mm)	Mass (T)	Surface/Volume (1/mm)
5	320	5.15e-5	0.81
10	320	2.06e-4	0.41
15	320	4.63e-4	0.27

2.2 Build Process Parameters

The parts under investigation were printed on an EOS M400 selective laser melting equipment in Inconel 718 under inert Argon atmosphere. The equipment uses a laser source at 300W with an approximate laser speed of 1000mm/s during build. Detailed process parameters are given in Table 2.

Table 2. Build process parameters

Powder type	Inconel 718	**Spot size**	~100 μm	**Scanning speed**	1000mm/s
Particle size	20-53 μm	**Power**	300W	**Hatch spacing**	0.11mm
Layer thickness	40 μm	**Platform Temperature**	80°C	**Rotation angle**	67°

The EOS M400 machine has a platform size of 400mm x 400mm, representing one of the largest commercial platform build sizes. The size of the platform influences the cooling behavior of the structure as a large platform increases the overall build time. This is illustrated in Figure 2. The build process consists of three sequential steps. Firstly, the platform is lowered to achieve the right build height per layer (40µm, see Table 2). Secondly, the powder is deposited and compacted with a rigid blade. Lastly, the laser source moves to melt the correct areas per layer. This process is repeated until the build process is completed.

Energy input only occurs during the laser exposure step, which can be relatively short in comparison to the other two processes of powder layer deposition and platform movement. It is therefore important to consider the relatively long cooling process following laser heating in order to accurately examine the process.

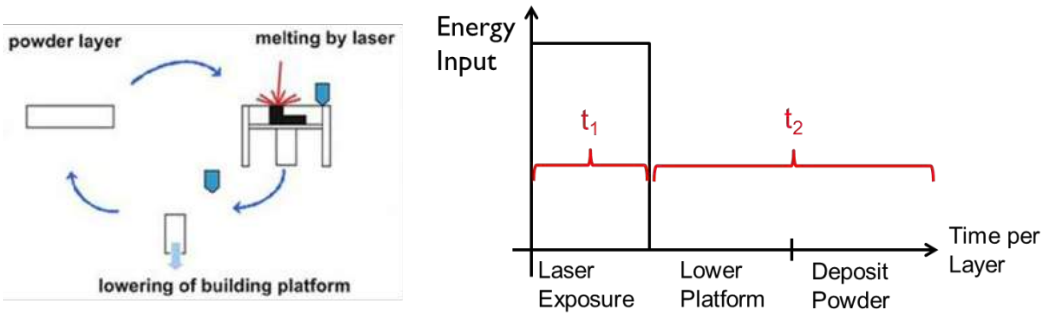

Figure 2. Two distinct time events during the build process.

Prior to printing, the approximate total print time is predicted by the machine's software. Table 3 shows the approximate building times for the three cylinders for the total height of 320mm. As expected, the powder recoating time is approximately equal for all three builds as this time only depends on the size of the platform and the speed of the blade distributing and compacting the powder. For a height of 320mm with 40µm layer height, we require 8000 layers to be built. Dividing the total recoating time by this number of layers, we calculate a merged cooling time considering both platform/recoating time of ~6.3s for every build layer.

Table 3. Effect of specimen volume on print duration

Diameter (mm)	t_1 Laser Exposure Time (hr:min:sec)	t_2 Powder Recoating Time (hr:min:sec)	$t_1 + t_2$ Total Printing Time (hr:min:sec)	$t_2 : t_1$ Ratio of cooling to heating time
5	00:33:41	13:58:57	14:32:38	24.91
10	02:01:12	13:59:36	16:00:48	6.93
15	04:21:24	14:00:15	18:21:39	3.21

From Table 3, we can also easily see that the ratio of cooling time to heating time changes drastically with changes in specimen volume. We expect this changing ratio to have a significant influence on the heat transfer problem. It should be noted that we can easily achieve the correct time for each event in the new Abaqus AM subroutines through the use of two separate event series as explained further in Section 3.

2.3 Solid Material Properties

The solid properties for Inconel 718 are obtained from general literature and summarized in Table 4. As mm units are chosen for the mesh, the units are converted to the standard N, mm, and T system. Temperature-dependent values were defined for most thermal properties. Thermal conductivity is a linear function of temperature. The specific heat shows a reduction in properties around the annealing temperature (~980°C [2]).

Table 4. Material properties of Inconel 718 (selected data points only)

Temperature [°C]	Density [T/mm^3] [2]	Specific heat [Nmm/TK]	Thermal conductivity [N/sK]	Latent heat [Nmm/T][4]
23	8.18e-9	4.6e8	11.2	2.89e11
200		4.78e8	14.1	
400		5.05e8	17.3	
600		5.38e8	20.5	
800		6.64e8	23.7	
1000		6.32e8	26.9	

2.4 Powder Properties

Inconel 718 powder has an average powder diameter of 20-53 um as given in Table 2. The compacted powder has an approximate volume fraction of 60%, a value which may be used to estimate the density and the specific heat of the material as shown in Table 5. Additionally, we define the Young's modulus and thermal expansion as significantly lower than the solid material as the powder particles are not connected and hence cannot carry any stresses.

Table 5. Powder properties of Inconel 718

Property	Specific heat	Density	Thermal conductivity
Value	$0.6*c_{p,solid}(T)$	$0.6*\rho_{solid}$	0.22W/mK (23°C)

However, this approach should not be used to determine the thermal conductivity of the material, a value which is instrumental when validating the effect of the surrounding powder particles on the temperature profiles within the solid parts during the build process. We performed in-house experiments with C-therm Tci, an equipment specifically designed for powder measurements, to determine the thermal conductivity of the powder at room temperature. The resulting value was 0.22W/mK as shown in Table 5. This very low value – when compared to the solid thermal conductivity - is explained as follows: due to the small contact areas between the neighboring powder particles with voids filled with air/inert argon, the thermal conductivity is governed by a more complex relationship described in earlier work by [2]:

$$k_e = \frac{\mu k_s}{1+\Phi\frac{k_s}{k_g}} \quad (1)$$

where k_s is the solid conductivity of the metallic powder and k_g is the conductivity of the gas filling the gaps between the powder particles. μ is the volume fraction of the solid. Φ is an empirical factor, which we fitted to our room temperature experimental value. In fact, it has been shown that most metal powders have very similar room temperature thermal conductivity values as determined by the gas filler.

The relationship in Equation 1 is assumed to hold until sintering temperature is reached. The relatively small increase prior to sintering temperature is due to the changes in thermal conductivity of gas and metal alloy with temperature. At the sintering point, particles start to fuse together and the contact area between particles increases [6]. Combining these two approaches, a temperature-dependent thermal conductivity was defined for Inconel 718 powder as per Figure 3.

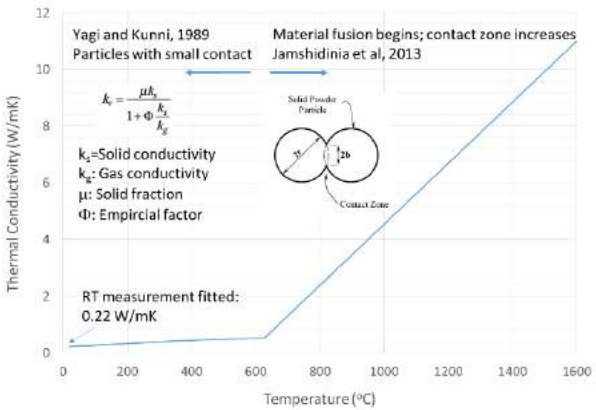

Figure 3. Thermal conductivity of powder material

3. Simulation Details

3.1 Additive Manufacturing Methodology

The additive manufacturing framework was released with Abaqus 2017. The key points of the modelling framework include the following steps: (1) Creating AM build part geometry as well as other potential parts such as build platform or surrounding powderbed, (2) re-creating machine print information such as laser scan path and powder recoating sequence, (3) during AM simulation, a new intersection module within Abaqus will progressively activate elements as per recoating process and (4) selection of adequate heating source (volumetric element representation or surface (node) based) to heat elements as per defined laser scan path. The new functionality automatically evaluates free boundary surfaces during the build process and assigns appropriate convection and radiation boundary conditions to the evolving surfaces. In the final step, a stress analysis is conducted based on the temperature output.

3.2 Heat Source Framework

Traditionally, the heat source movement has been implemented as a volumetric distributed element heat flux as per Goldak's semi-ellipsoid model [7]. Assuming no eccentricity (i.e. circular distribution) for the heat source on the surface, the laser heat source distribution is described as

$$Q(x,y,z,t) = \frac{2P\eta}{r^2 d\pi\sqrt{\pi}} \exp\left[-\left(\frac{(x+v_x t)^2}{r^2} + \frac{(y)^2}{r^2} + \frac{(z)^2}{d^2}\right)\right] \quad (2)$$

where the *x*-axis aligns with the laser moving direction, P is the nominal laser power, η is the absorption coefficient and v_x is the moving speed of the laser and t is the time. The other dimensions are defined by laser source parameters, such as laser spot size radius r and powder penetration depth d. This approach requires a very fine mesh in the order of at least one element per build layer to resolve the volumetrically distributed heat flux accurately. A total of 9-16 elements within the distributed heating volume are suggested for mesh convergence. With these restrictions, this approach is useful to establish detailed temperature profiles and microstructure evolution for relatively small build volumes, but will require very long simulation times for typical AM parts.

Alternatively, a faster modelling approach is implemented, in which the heat energy due to the moving heat source is now interpreted as a distributed surface heat flux for a given time increment and is assigned to the respective top surface nodes of the latest activated element layer. The AM manual and workshops are currently specifying ~10-20 build layers per element as appropriate resolution. This results in an approximate mesh size of 0.5-1.0mm for an adequate mesh for AM parts with 40μm build layer height.

3.3 Nodal Flux Simulation

Several types of model set-ups were investigated with increasing modelling complexity to establish best practice guidelines for SLM processes:

a) AM part only with temperature boundary conditions at z=0mm (position of build platform) and radiation/convection cooling
b) AM part with surrounding powder particles with temperature boundary conditions at z=0mm (top surface of build platform) and radiation/convection cooling
c) AM part with surrounding powder particles and build platform with temperature boundary conditions at the bottom of the build platform and radiation/convection cooling

The solid part and surrounding powder region were modelled within one part with adequate partitions. 3D solid hex heat transfer elements (DC3D8) were chosen for the simulation. The platform is not considered part of the AM build, hence may have a coarser mesh compared to the build part. The two parts are coupled together via *TIE constraints, hence enforcing the same temperatures at the interface. Figure 4 shows the schematics for the most complex model set-up:

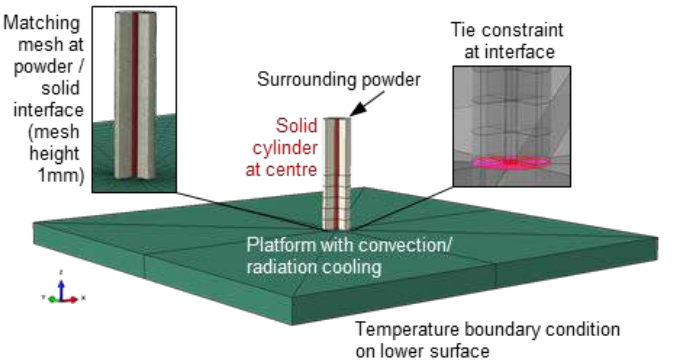

Figure 4. Model set-up with build platform

The powder bed (nodal flux) simulation process was chosen in the AM modeler in order to allow for faster simulation time of the full structure. For this heating process a coarser mesh may be used as outlined in Section 3.2, with the AM manual and workshops currently specifying ~10-20 layers per element. This results in an approximate mesh density of 0.5mm for an adequate mesh with 40μm layer height.

The build height was capped at a height of 100mm as initial simulations showed self-similar heating and cooling profiles at this point, which were independent of the height. The following thermal boundary conditions and initial conditions were specified: (1) pre-heated platform condition of 80°C for the initial platform condition and lower platform boundary condition, (2) 26°C for surrounding temperature and initial powder temperature as the powder is not preheated in the SLM hopper and hence is assumed to enter at room temperature and (3) a radiation and film convection coefficient to ambient argon atmosphere. The radiation coefficient was kept constant at ε=0.45 without additional calibration. A suitable film coefficient for heat transfer to air/inert atmosphere is suggested as h=0.018 Nmm^{-1} s^{-1} K^{-1}. This film coefficient selection does not consider the speed of the moving gas across the top surface.

3.4 Laser Path and Powder Deposition Event Series Generation

A script was generated to allow for laser path calculation for cylindrical and rectangular cross-sections according to the values given in Table 2. The hatch spacing was used to determine the line spacing of the laser movement. The spot size radius was used to determine a suitable spacing between the end of the laser path and the surrounding geometry boundary. The known laser speed was then used to determine the relevant time points. For each subsequent build layer, a rotation angle of 67° was applied. Two resulting exemplary scan patterns highlighting the changing laser path orientation are shown in Figure 5. It should be noted that the same laser movement event series can be applied for both nodal flux processes and detailed Goldak meltpool simulation.

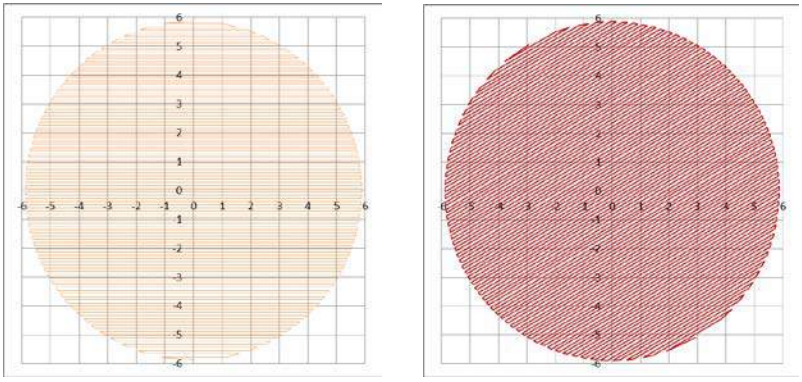

(a) **(b)**

Figure 5. Exemplary laser movement for circular cross section with varying orientation of (a) θ = 0° and (b) θ = 30°

The recoater movement was specified in a second event series. The given time periods in both event series guarantee sequential processes similar to the real build process. The powder deposition process is scheduled to take 6.3s for each layer independent of the laser movement as discussed and highlighted in Table 3. As the laser source is switched off during the recoating process, the structure will continue to cool during this time. As previously discussed, this is an important point to consider during the simulation.

3.5 Energy Balance

In order to validate the nodal flux model set-up with appropriate laser input, a simple energy balance was derived for the cylinder model with D=5mm. For this approach, no thermal boundary conditions are specified, hence all energy input is converted into stored energy. To simplify the analytical calculations, a constant specific heat was specified and latent heat was omitted. The energy balance is given via

$$m * c_p * \left(T_{final} - T_{air}\right) = P * t * \varepsilon \quad (3)$$

Where m is the mass of the cylinder, c_p is the specific heat, T_{final} is the final temperature of the cylinder at the end of the build process simulation and T_{air} is the surrounding air temperature. P is the laser power, t is the time of the laser power input during the build and ε is the absorption coefficient as specified for the laser input. The final temperature following build for the D=5mm model for a build height of 100mm was 3813.6°C. This constant final temperature is independent of increment size and mesh size. The energy balance error was determined to be 0.4% for the given material parameters in Table 4 (constant specific heat value). Additionally, it should be noted that the final temperature was significantly above the melting temperature of Inconel 718 (~1400°C), indicating that the power input is sufficient to cause solidification of the powder material. The later introduction of thermal boundary conditions to allow for radiation, convection and conduction will lead to a significant reduction of this maximum temperature.

3.6 Mesh Size Refinement for Nodal Flux Model

In order to establish the effect of mesh size refinement, the cylinder model with D=5mm was initially investigated with a coarse time incrementation of 1 increment/layer (~6.46s). While this time increment does not give realistic peak temperature values due to the significant cooling time (~6.3s, see Figure 2), it is an adequate approach to investigate the effects of decreasing element size on the overall temperature predictions. Mesh size refinement studies were initially undertaken for a mesh size of 1.5mm, 1.0mm and 0.5mm (see Figure 6).

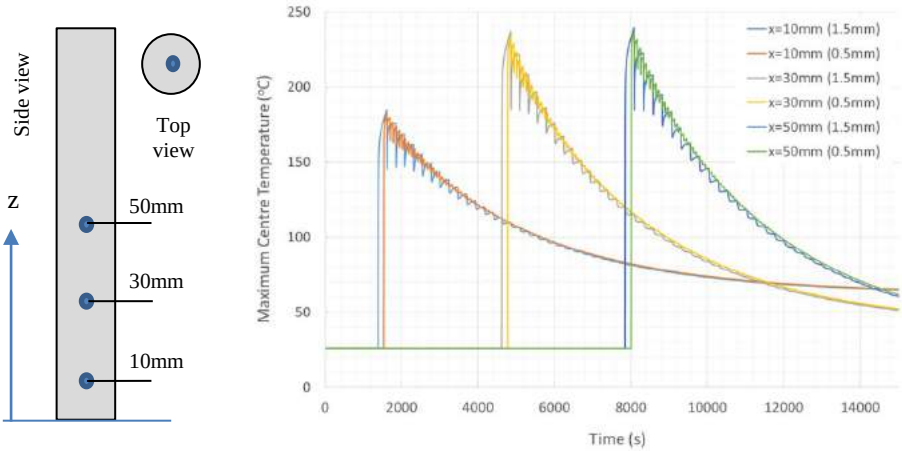

Figure 6. Effect of mesh refinement on peak temperature history

For the same time increment, the peak temperatures per laser pass at the center of the cylinder for different cylinder heights are not affected by the mesh refinement, as shown in the figure. However, the temperature drop following addition of the next layer increases with a coarser mesh. For each added layer, a corresponding temperature drop is observed. The finer mesh has a larger number of element layers and hence the temperature drops occur more frequently, but by a smaller

amount. This is expected as conduction occurs into the volume of the new element layer and its total outer surfaces are also activated to conduct and radiate heat to the surrounding material. Further improvement to alleviate excessive temperature reductions are expected with the upcoming release of partially-activated elements during the heat transfer analysis.

3.7 Influence of Surrounding Powder

Preliminary investigations with varying amount of powder surrounding the build part were undertaken. The time increment size was chosen as 1 increment/layer deposition to allow for adequate computational effort. This results in a fairly coarse temperature prediction, but enables the determination of the influence of the surrounding powder particles based on maximum temperatures achieved per layer in an efficient manner. The powder properties were given in Table 5 and Figure 3. Assuming that the area of surrounding powder is chosen large enough, temperatures in the powder immediately surrounding the solid will conduct heat, but areas further away will remain close to room temperature due to the effects of top surface convection. Heat can also be conducted to the building platform via the powder material. The film coefficient from the powder bed to the surrounding ambient air is assumed to be 0.018W/mK as shown in Figure 7. For the surrounding powder material, heat transfer into the material is clearly visible. The temperature then reduces towards the outer edge of the simulated surrounding powder material.

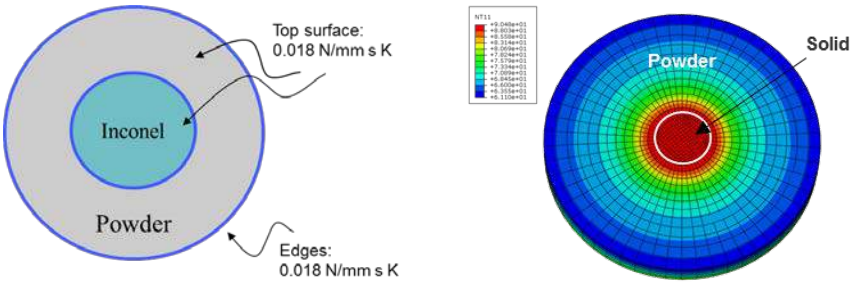

Figure 7. Model with solid/powder region and resulting temperature distribution

Results showed that converging temperature profiles were obtained once the diameter of the surrounding powder was around 3x-5x of the solid part. All models presented in the later sections are run with surrounding powder layers as per Table 6. In an attempt to reduce computational time, equivalent film coefficients were also calibrated for two of the solid cylinders without surrounding powder to achieve similar maximum peak temperatures as for the respective parts with the surrounding powder. It can be seen in Table 6 that the equivalent film coefficients can be significantly higher than the value normally specified on the AM surface for convection to inert atmosphere (h=0.018 N mm^{-1} s^{-1} K^{-1}). This shows that the powder bed has significant capacity to act as a heat sink, which increases cooling rates. However, the equivalent film coefficient was found to depend on the part geometry and especially the ratio of surface-to-volume changes. The calibration approach therefore needs to be repeated for each new part geometry to be modelled.

Table 6. Powder dimensions surrounding solid part

Diameter [mm]	Diameter powder [mm]	Equivalent film coefficient solid only [N mm^{-1} s^{-1} K^{-1}]
5	25	0.05
10	30	0.03
15	45	--

3.8 Influence of Time Incrementation

Small time increments are required to resolve the rapidly evolving temperature changes during laser movement periods. A shorter time increment results in a more concentrated hot spot (see Figure 8). This is due to the fact that temperature equilibrium is established for any given time increment. This especially affects the peak temperature per laser pass through the layer. A smaller time increment therefore results in significantly increased peak temperatures. For the given process and simulation parameters (laser speed, heat source type, minimal mesh size), a time increment of 10ms is considered the best solution as the distributed surface heat flux becomes uneven for further increment reductions.

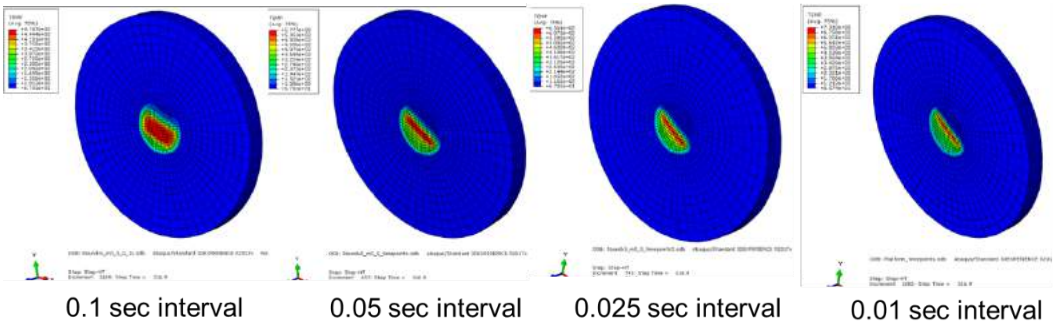

Figure 8: Contour plots at the same total step time achieved with decreased time increments, resulting in decreasing hot spot size and peak temperatures increase.

Figure 9 (a) shows the peak temperatures per laser pass as a function of increment size for layers 13-24 (height 0.5mm – 1mm). It can be seen that the peak temperatures for Δt=10ms and Δt=25ms start to approach similar temperatures. The decay is also captured fairly accurately (Figure 9 (b)).

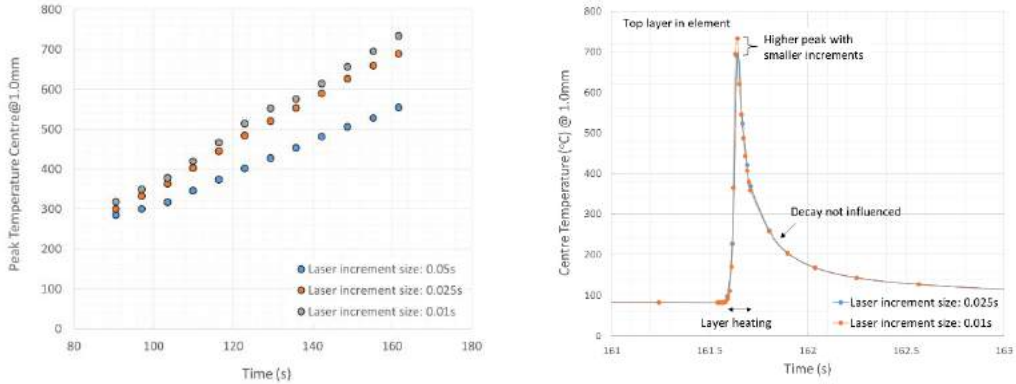

(a) **(b)**

Figure 9: (a) Peak temperature per laser pass depending on laser increment size and (b) time-temperature graph for two laser increment sizes.

It was observed that it is less important to resolve the cooling period with the same increment size for accurate temperature predictions. This approach is outlined in Figure 10. Different time incrementation schemes are chosen for the two event series, with suitable values selected at Δt=10-25ms for the laser movement and 1.5s for the recoating process. This approach results in very good temperature resolution for the heating phase, while still capturing the cooling phase. In order to avoid defining separate steps for the two events for each layer, a better way to achieve this type of adaptive time increment strategy is through the use of individually specified timepoints. Respective files are created in Excel and included as separate input files for the analysis.

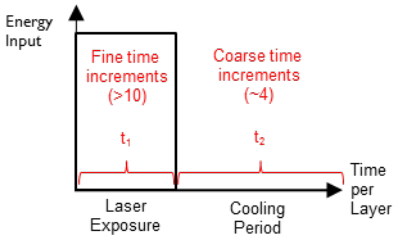

Timepoints example

1.5,3,4.5,6,6.3,6.325,6.35,6.375
6.4,6.425,6.45,6.46836,7.96836,9.46836,10.96836,12.46836
12.76836,12.79336,12.81836,12.84336,12.86836,12.89336,12.91836,12.93672
14.43672,15.93672,17.43672,18.93672,19.23672,19.26172,19.28672,19.31172
etc

(a) **(b)**

Figure 10: Smart time incrementation for separate event series.

3.9 Influence of Build Platform

The platform acts as a finite heat sink during the additive manufacturing process. Its temperature is controlled at the bottom surface via a thermocouple. For the numerical simulation, the platform's size was simulated as 400mm x 400mm x 20mm. The temperature condition of 80°C was specified at the bottom surface of the platform. Additional film coefficients simulating convection to air were included for edges and top surface of the platform. During the simulation, no change of peak temperatures during the laser pass were observed given the same time incrementation and

mesh size as shown in Figure 11. However, for the cooling period, a significantly slower and more realistic decay approaching the boundary condition of 80°C was found. Including the build platform had the additional advantage of improving the convergence during the initial cooling increment. For small time increments of Δt=10ms, convergence with fixed time incrementation was not possible without the platform. Changing to adaptable time increment size resulted in significant increase of computational time. It was therefore computationally more accurate, but also faster, to include the platform during simulation.

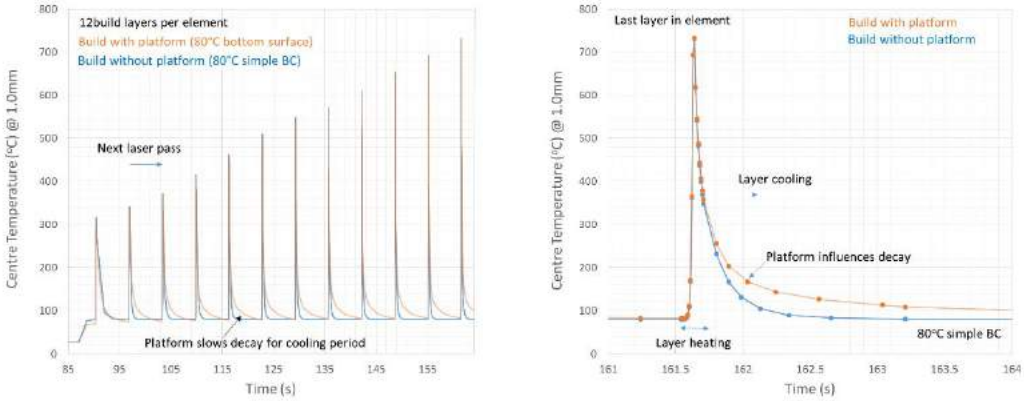

Figure 11: Effect of platform cooling for (a) one element with repeated laser passes and (b) last pass of element in high resolution at z=1.0mm.

3.10 Comparison to Goldak Model

Figure 12 shows a direct comparison for the same total step time and same time incrementation of the contour plots obtained for the Goldak model and the nodal flux model. Firstly, it can be seen that the finer mesh of course leads to a better resolution of the temperature field. However, the coarse mesh shows a visually very similar temperature field with good agreement of the hottest surface region during laser source movement.

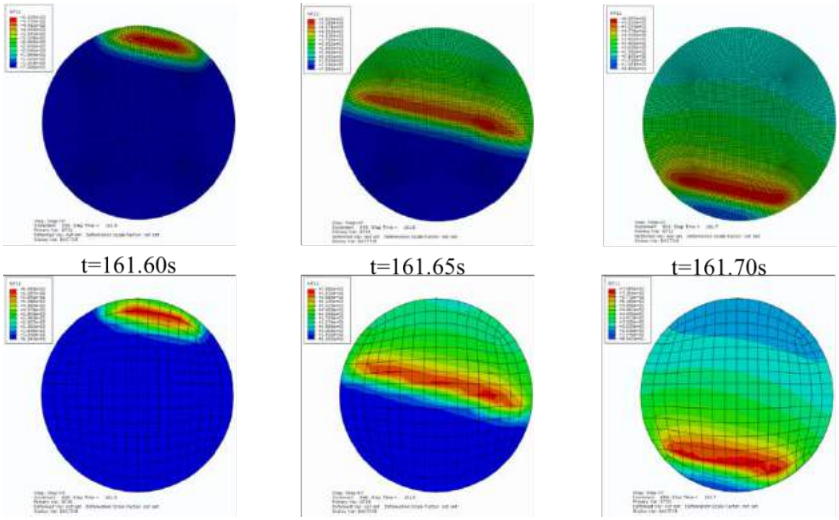

Figure 12. Contour temperatures for 5mm cylinder at z=1mm from platform with 25 layers activated for the Goldak model (mesh height 40μm) (top row) and 2 layers activated for the nodal flux model (element layer height 0.5mm) (bottom row).

Figure 13 shows the comparison of Goldak laser temperatures with the nodal flux model at the center of the 5mm diameter cylinder for a height of 1mm as a function of time. Both models register temperature spikes at the same time frequency determined by the supplied event series.

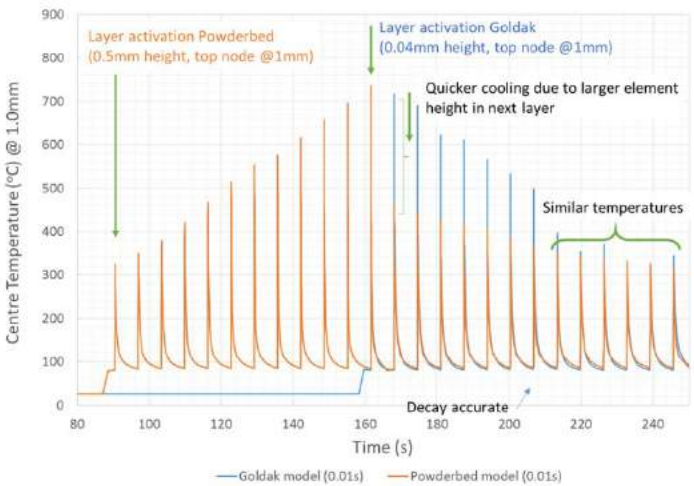

(a)

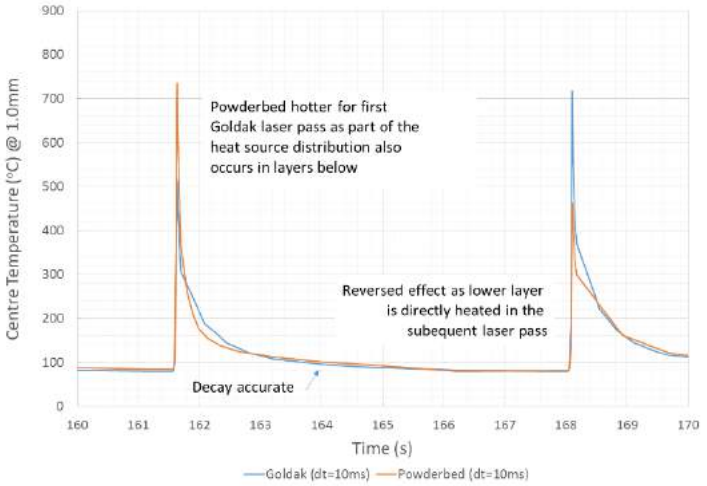

(b)

Figure 13. Temperature history comparison for Goldak and nodal flux model

A few things are noted: the nodal flux approach will register temperature spikes at the center node at 1mm height earlier (~90s) as the element size along build height is larger. As such, 12 laser passes are completed per element and distributed via the same surface nodes, while only one laser pass is completed per element for the Goldak model as seen in Figure 13(a). For the Goldak model, the element connected to the node at 1mm is activated at 160s. Following the activation of the Goldak model, the peak temperature at 1mm are similar as shown in Figure 13(b) in more detail, but the subsequent peak temperatures are higher. This is due to several facts: (1) the next element layer activation for the nodal flux model introduces a larger surface area for heat convection and radiation as well as a larger element volume for heat to conduct into (this was also noted for the mesh refinement studies); (2) the Goldak model is a volumetric model, and the energy is distributed over the volume of several element layers (penetration depth=150μm). Hence some heating occurs further away from the top surface and the cooling boundary effects. For the later passes, the temperatures spikes then become similar as highlighted in the figure.

Overall, the comparison shows that the results for the Goldak and nodal heat flux model are similar given the same time incrementation and resolution of laser movement. This increases user confidence in the new modelling approach.

4. Discussion

4.1 Influence of Build Height and Cylinder Width on Microstructure and Mechanical Properties

Figure 14 shows the differences in mechanical properties when tested at various heights for the various build diameters. z=0mm corresponds to the height of the platform. The variation in mechanical properties is attributed to differences in microstructure, which in turn are due to differences in cooling rates as a result of build height and specimen dimensions. Scanning electron microscopy (SEM) taken at higher resolution from the side surfaces reveals columnar γ–phase dendrite formation. These columns align themselves with the steepest temperature gradient during manufacture (z-direction). Statistical analysis reveals differences in the dendrite column thickness: the columnar dendrite thickness of cylinders with 15 mm diameter is much smaller than for the two thinner samples. It is noted that the thickness histogram also changes along the building direction: the columnar dendrite thickness close to the building platform is much finer than that at higher build heights. A finer columnar width is the result of higher cooling rates between melt temperature and relevant phase transformation temperatures. Transmission electron microscopy (TEM) additionally reveals the presence of a carbide phase in the lower part of the D=15mm cylinder. Carbide phases are also generated during high cooling rates. Both findings point towards higher cooling rates for this sample in the lower build region, which is consistent with the UTS measurements.

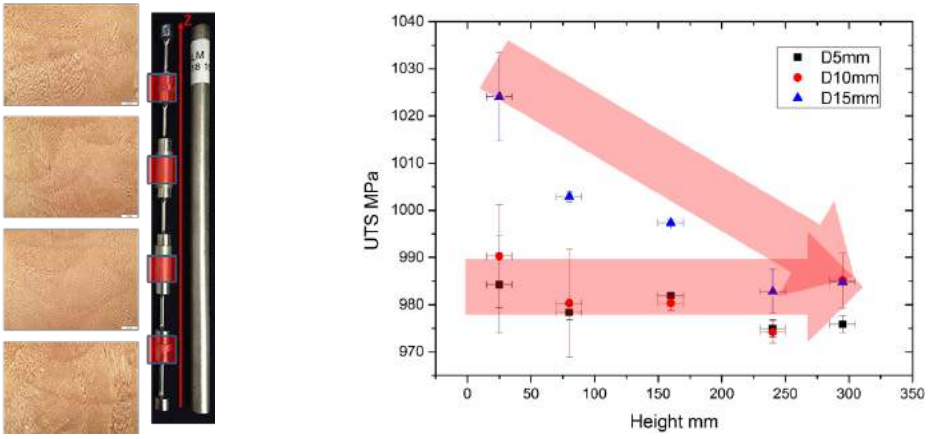

(a) **(b)**

Figure 14. (a) Built test specimen and microstructure (50x magnification) and (b) difference in mechanical properties as function of building height and cylinder diameter

4.2 Temperature Profile Analysis

Several conclusions could be drawn based on the presented experimental results: (1) cooling rates are higher closer to the platform, (2) the platform effect is limited to below z=50mm for D=5mm and D=10mm, while properties continue to vary up to z=250mm for D=15mm and (3) differences in material properties and hence cooling rates are most pronounced for cylinders with D=15mm diameter. To achieve detailed cooling rates for the build volume and height from the experimental parts is not possible with the Goldak model within a reasonable computational timeframe. Hence focus was given to the results from the nodal flux model instead.

In the following, we examine the temperature distributions via temperature history plots and contour plots for the three cylinder dimensions. Simulations were run up to a build height of 100mm or until self-similar temperature profiles with build height were obtained. While no detailed microstructural prediction is possible at this point due to the complex heating, cooling and reheating process, the influence of the change in geometry on the temperature profiles is evident. Figures 15(a)-15(c) show the temperature-time history as a function of build height for selected center points with their distance from build platform indicated. Figure 15(d) summarizes the peak temperatures as a function of build height and cylinder diameter. At lower build heights, heating rates will be faster as shown by the initially lower peak temperatures. The reduction in peak temperature for the same time increment can be attributed to faster re-distribution (cooling) of temperatures within the build volume, platform and surrounding powder material. Temperature profiles then become self-similar as the heat sink effect from the platform is minimized. It is shown that the height required for self-similar temperature profiles increases with cylinder diameter. The cooling rates stabilize at a height of 30mm and ~70mm for a diameter of 5mm and 10mm, respectively, while for a cylinder of 15mm they still have not stabilized for the height of 90 mm. For the cylinder of 15mm, the cooling rates close to the platform are significantly higher as evidenced by the significantly lower peak temperature. This is consistent with the experimental results. The increased build height for self-similar temperature distribution with cylinder diameter is also consistent with the experimental results. We also observe that this trend reverses slightly for increased building heights, which is currently not evident from experimental results.

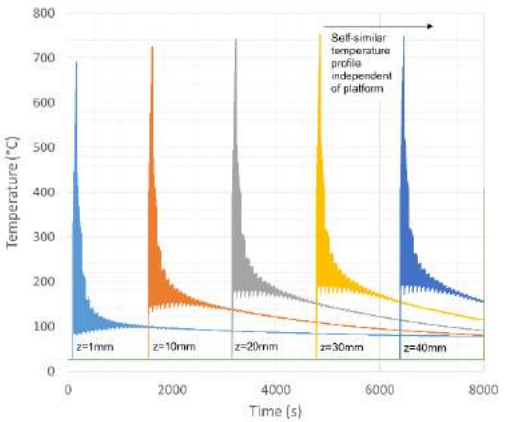

(a)

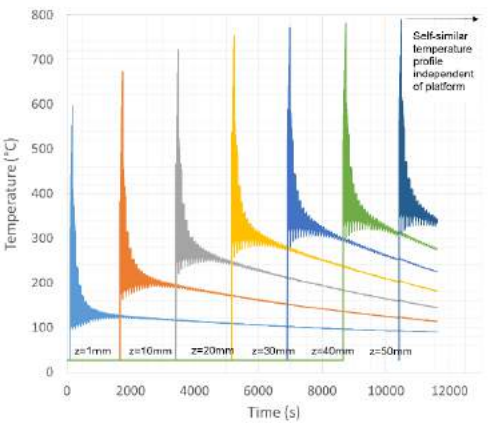

(b)

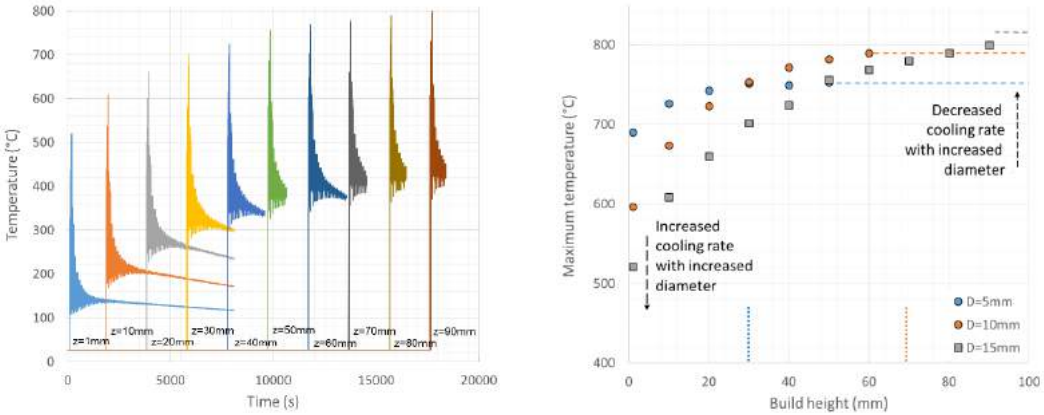

(c) (d)

Figure 15. History plot for center temperatures at various heights for cylinder heights of (a) 5mm cylinder, (b) 10mm, and (c) 15mm. (d) shows the influence of cylinder diameter and build height on peak temperatures and cooling rates.

Figure 16 shows that the hot spot heat distribution is much narrower for the larger diameter cylinder for the same time increment. This is due to the fact that the smaller diameter allows overlapping of several neighboring scan paths for the same time period compared to the larger diameter cylinder. While it is not obvious from the contour plots, the logical conclusion is that the larger cylinder diameter results in faster spot cooling during laser movement due to increased heat conduction to the platform as also observed from temperature-time histories in Figure 15. Further analysis of the temperature results is on-going.

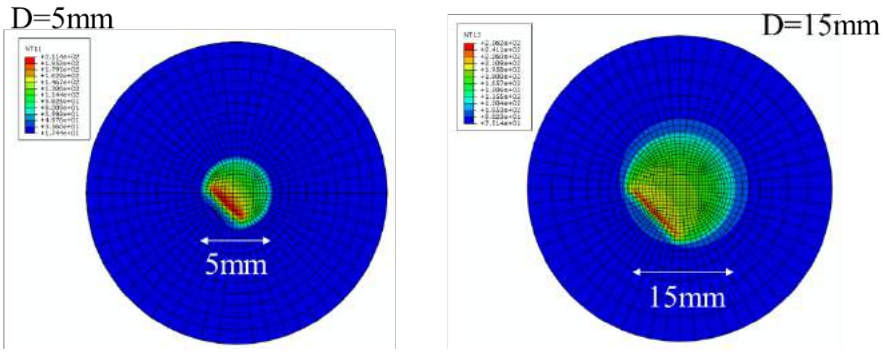

Figure 16. Temperature distribution in solid part for two different diameters for the same laser increment size and same element layer/laser pass.

5. Conclusions and Outlook

The current AM modelling framework is still undergoing continuous further development, and the research findings were discussed regularly with the Dassault Systemes team. Several new features for AM processing will be available shortly, namely

- partial element activation to alleviate the problem of larger temperature drop observed for the coarse mesh structure in comparison to a fine mesh;
- possible definition of separate time increments for the event series, eliminating the need for separate timepoint input creation; and
- improved sequential output transfer from temperature to stress analysis. Large temperature .odb files are currently slowing down the stress analysis step or leading to errors due to a maximum allowable data amount.

Based on presented temperature analysis results with the nodal flux model, it is clear that this simulation approach allows the determination of temperature profiles even for larger models at a reasonable computational expense. Several conclusions could be drawn based on the presented results:

- an approximate film coefficient may be calibrated to eliminate modelling of the surrounding powder material. The calibrated value will depend on the specimen geometry (surface / volume ratio);
- the surrounding powder bed acts as a significant heat sink for specimens with high surface-to-volume ratio as established by the calibrated film coefficient. This effect should be included;
- it is also important to model the build platform during AM process simulations to improve temperature convergence and capture heat sink effects;
- the build platform acts as an accelerator for cooling rates close to the platform and this effect depends on the specimen geometry; and
- inclusion of the powder material has some effects on the cooling rates for the SLM process, but is considered less important than the build platform effect. However, for other powder bed processes, such as electron beam melting, the powder temperature is at around 600°C, in which case the thermal conductivity of the partially-sintered powder can be significantly higher. This will be further investigated in future work.

Lastly, further work needs to be undertaken in order to relate the temperature output to the observed microstructure findings. Future work will then concentrate on the subsequent stress analysis for printed Inconel 718 structures.

6. Acknowledgement

The SIMTech authors would like to thank the Agency for Science Technology and Research and the Science and Engineering Research Council for support of this work (SERC Grant nos 1325504102 and 1426800088).

References

1. X. Tan, Y. Kok, Y. J. Tan, G. Vastola, Q. X. Pei, G. Zhang, et al., "An experimental and simulation study on build thickness dependent microstructure for electron beam melted Ti–6Al–4V," Journal of Alloys and Compounds, vol. 646, pp. 303-309, 10/15/15 October 2015 2015.
2. Material data sheet, EOS NickelAlloy IN718, downloaded March 2017.
3. C.R. Brooks, M. Cash and A. Garcia, The heat capacity of Inconel 718 from 313 to 1053K, Materials Science, 10, 419-421, 1978
4. F. Klocke and C. Wagner, Direct Selective Laser Sintering of Superalloys, Solid Freeform Fabrication Symposium, Austin, Texas, USA, 2002
5. S. Yagi and D. Kunni, Studies of Effective Thermal Conductivities in Packed Beds, American Institute of Chemical Engineers (AiChE) Journal, 3(3), 373-381, 1989
6. M. Jamshidinia, F. Kong, R. Kovacevic, Numerical Modeling of Heat Distribution in the Electron Beam Melting of Ti-6Al-4V, Journal of Manufacturing Science and Engineering, 135, 061010-1- 061010-14, 2013
7. J. Goldak, A. Chakravarti and M. Bibby, A new finite element model for welding heat sources, Metallurgical Transactions B, 15B, 299-305, 1984